Hybrid deep belief network and fuzzy clustering approach for geothermal prospectivity mapping in northeastern Nigeria using magnetic and landsat data

A. K. Usman[a,b,d,*], Y. A. Hassan[a], A. A. Bery[c,d], A. A. Sunny[c,d], M. D. Dick[c,d], A. B. Mohammed[c,d], R. O. Aderoju[e]

[a]*Department of Physics, Faculty of Physical Sciences, Ahmadu Bello University, Zaria, Nigeria*
[b]*Department of Engineering Geology, Hydrogeology and Applied Geophysics, Faculty of Natural Sciences, Comenius University, Ilkovičova Bratislava, Slovakia*
[c]*Geophysics Programme, School of Physics, Universiti Sains Malaysia, 11800 USM, Penang, Malaysia*
[d]*Earth System Processes and Hazard Modeling Lab, Geophysics Programme, School of Physics, Universiti Sains Malaysia, 11800 USM, Penang, Malaysia*
[e]*Geology Department, University of Georgia, USA*

Abstract

Nigeria faces persistent energy supply challenges, particularly in its northeastern region, where grid access is limited and dependence on fossil fuels undermines sustainability goals. Although the National Renewable Energy Action Plan (NREAP 2015–2030) outlines ambitious targets for renewable energy integration, it notably lacks specific strategies for geothermal development—leaving a critical gap in policy and resource utilization. This study addresses that gap by developing a scalable, cost-effective geothermal prospectivity mapping framework using remote sensing and aeromagnetic data integrated through a hybrid machine learning model. A novel combination of Deep Belief Networks (DBN) for feature extraction and Fuzzy C-Means (FCM) clustering for spatial classification was employed, with optimization achieved using three metaheuristic algorithms: Genetic Algorithm (GA), Particle Swarm Optimization (PSO), and Simulated Annealing (SA). Among these, the DBN-SA model achieved the best internal validity, with superior Silhouette Score, Davies–Bouldin Index, and cluster compactness, ensuring robust and interpretable prospectivity results. Key geothermal indicators—including land surface temperature, vegetation stress, Curie depth, heat flow, and magnetic source depth—were derived from Landsat and airborne magnetic datasets. The resulting map classifies the study area into low, moderate, and high geothermal potential zones, with validation supported by geological correlation and the presence of known thermal features like the Wikki Warm Spring. Approximately one-third of the area was identified as high-potential, particularly over basement terrains with high heat production and structural permeability. This approach offers both scientific insight and practical direction for decentralized, low-carbon energy deployment in northeastern Nigeria, aligning with broader national renewable energy goals and filling a crucial gap in geothermal resource planning.

Communicated by: Peverga R. Jubu

1. Introduction

The global demand for energy is steadily increasing due to rapid population growth, industrialization, and technological advancement [1]. Energy generation is fundamental to socio-economic development, playing a crucial role in enhancing the well-being and prosperity of individuals, communities, and nations [1]. However, limited access to reliable energy exacerbates poverty, underdevelopment, and economic instability, particularly in developing countries [2]. According to the 2016 World Energy Resources Report, fossil fuels still constitute around 81% of global energy consumption. While they have historically fueled industrial and infrastructural progress, these sources are finite and are major contributors to greenhouse gas emissions. Misra and Kalra [3] note that such emissions are linked to ozone layer depletion, global warming, and erratic climate behavior—raising significant concerns about environmental sustainability. Considering these challenges, renewable energy sources—such as solar, wind, hydroelectric, biomass, tidal, wave, and geothermal—offer cleaner, more sustainable alternatives [4, 5]. Among these, geothermal energy stands out due to its reliability, low environmental footprint, and independence from fluctuating climatic conditions [5, 6]. It remains largely unaffected by temporal changes in solar radiation, wind, or water availability, making it both cost-effective and environmentally friendly energy source [2, 7]. Recent global efforts have explored geothermal potential using various techniques and datasets, including geological, geochemical, geophysical, borehole, and remote sensing data [8, 9]. Multicriteria Decision Analysis (MCDA) methods such as Analytic Hierarchy Process, Fuzzy Logic, ELECTRE III, PROMETHEE II, and Evidential Belief Functions have shown promise in geothermal prospectivity mapping [5]. However, traditional MCDA approaches often assume deterministic or linear relationships, which may not adequately reflect the inherently nonlinear and uncertain nature of geothermal systems [5]. To overcome these limitations, machine learning (ML) techniques have emerged as powerful tools capable of modeling complex, nonlinear relationships among geothermal indicators without requiring extensive expert input. The Deep Belief Network (DBN) has been successfully applied in various geoscientific tasks, such as groundwater potential mapping and landslide susceptibility analysis [10–12]. DBN's performance can be further enhanced by integrating metaheuristic optimization algorithms that fine-tune its internal parameters [13, 14]. Popular metaheuristics such as Genetic Algorithm (GA), Particle Swarm Optimization (PSO), and Invasive Weed Optimization (IWO) have demonstrated improved results when combined with Adaptive Neuro Fuzzy Inference System (ANFIS) [5, 10, 15]. In this study, three hybrid models—GA-ANFIS, PSO-ANFIS, and IWO-ANFIS—were developed to integrate geophysical and remote sensing datasets for geothermal potential assessment. These models aim to address the nonlinear complexity of geothermal systems, minimize subjectivity in decision-making, and enhance predictive accuracy. The Receiver Operating Characteristic–Area Under the Curve technique was used for model validation.

Some studies have been carried out on geothermal potential in different basins and geological area in Nigeria [16–18]. Adedapo *et al.* [19] and Emujakporue and Ekine [20] reported subsurface temperature analyses showing a minimum geothermal gradient of 1.2°C/100 m in the central part of the basin and a maximum of 7.62°C/100 m in the northeastern part. Obande *et al.* [21], in their literature reviews, noted signs of crustal thinning in the Upper Benue Trough and suggested the presence of anomalously hot material at relatively shallow depths. Kasidi and Nur [22] estimated the Curie Point Depth (CPD), heat flow, and geothermal gradient using aeromagnetic data over Jalingo, northeastern Nigeria. Their results showed CPD values ranging between 24 km and 28 km, geothermal gradients between 21°C/km and 23°C/km, and heat flow values from 53 mW/m^2 to 61 mW/m^2. Kwaya *et al.* [23] also observed geothermal gradients in the Nigerian sector of the Chad Basin ranging from 28.1°C/km to 58.8 °C/km, with corresponding heat flow values between 45 mW/m^2 and 90 mW/m^2. In contrast, Chukwu *et al.* [24], focusing on parts of the eastern Niger Delta Basin, found very low heat flow values and concluded that the area has limited potential for geothermal resource exploitation. This study introduces a novel hybrid machine learning workflow that combines Deep Belief Networks (DBN) for deep feature extraction with Fuzzy C-Means (FCM) clustering, optimized using metaheuristic algorithms (GA, PSO, SA), for geothermal prospectivity mapping. It is the first to apply this unsupervised, data-driven approach in Northeastern Nigeria, integrating multisource geophysical and remote sensing datasets to uncover hidden geothermal patterns. The workflow is fully reproducible, leveraging standard preprocessing, open-source tools (e.g., ArcGIS, Python/Jupyter), and internal validation metrics, making it adaptable for geothermal exploration in other data-sparse or underexplored regions.

1.1. Geothermal energy in Nigeria: context and challenges

In the Nigerian context—particularly in the northeastern region—energy supply remains inadequate and unstable, underscoring the need to explore local, sustainable alternatives. Geothermal energy, derived from Earth's internal heat, offers an eco-friendly solution to the country's energy challenges and aligns with global clean energy goals [21, 25–27]. The region's tectonic framework, lithological heterogeneity, and structural features suggest promising geothermal potential, yet these remain largely uninvestigated [28]. Traditional geothermal exploration techniques—such as detailed fieldwork, borehole drilling, and high-resolution geophysical surveys—are expensive, time-consuming, and often impractical in remote or conflict-prone areas [29]. In contrast, integrating remote sensing and geophysical datasets with machine learning models offers a scalable, cost-effective approach for preliminary geothermal mapping. For instance, Landsat-derived thermal and spectral indices, when combined with magnetic data, can high-

---
*Corresponding author: Tel. No: +234-816-459-4389;
Email address: ahmedkehindeusman@gmail.com;
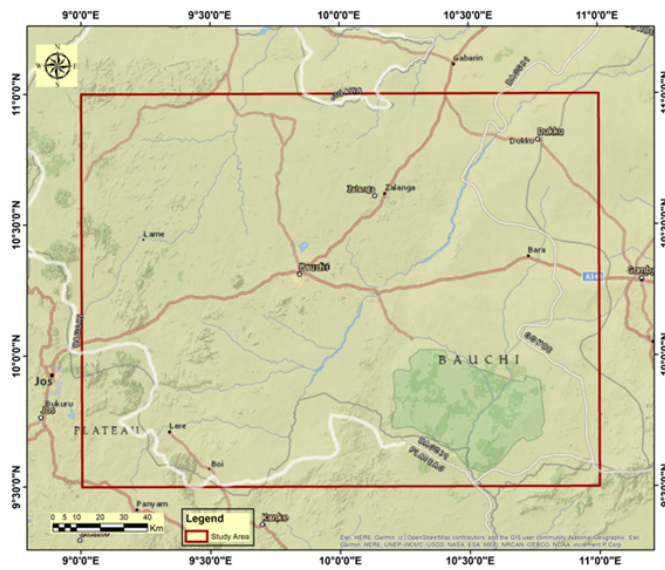akusman@abu.edu.ng (A. K. Usman)
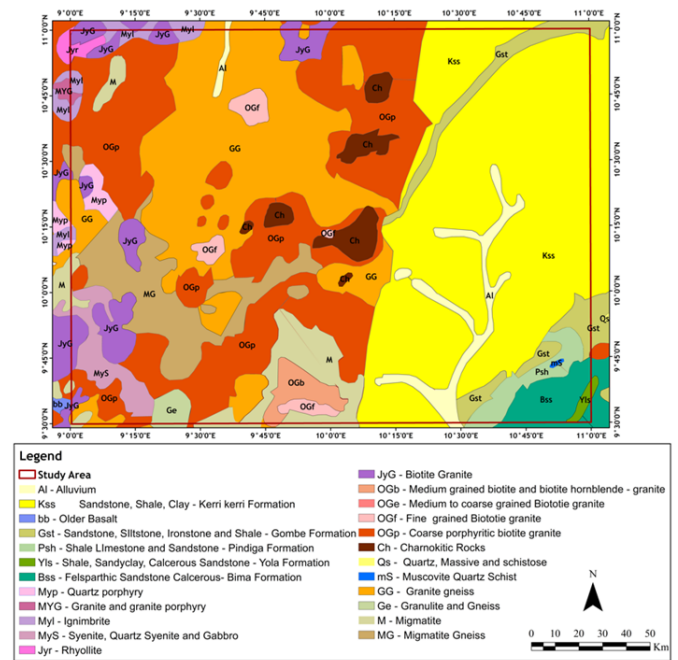
Figure 1. Location map of the study area.

Figure 2. Geological map of the study area.

light geothermal surface manifestations like thermal anomalies, hydrothermal alterations, and structural lineaments [27]. Despite Nigeria's National Renewable Energy Action Plan, which aimed to increase renewable energy integration to 23% by 2020 and 31% by 2030, implementation has been hampered by overlapping mandates and poor collaboration among key agencies such as the Energy Commission of Nigeria, the Nigerian Electricity Regulatory Commission, and the Ministry of Power. Notably, the plan lacks specific provisions for geothermal energy development. This omission has resulted in policy neglect, the absence of targeted incentives, and weak institutional coordination for geothermal exploration. Consequently, geothermal energy remains underutilized, despite its significant potential, particularly in regions like Northeastern Nigeria. Recent studies [26, 27, 30–34] highlight favorable geothermal conditions across various regions, identifying low CPD and high heat flow (HF) as key indicators of geothermal prospectivity.

1.2. Advancing geothermal mapping with hybrid machine learning

Machine learning algorithms excel at detecting complex spatial patterns in high-dimensional data. Deep Belief Networks (DBNs), which consist of stacked Restricted Boltzmann Machines, are especially effective for unsupervised feature extraction and nonlinear classification [35, 36]. DBNs can uncover hidden relationships among geothermal indicators but may not fully address the uncertainty inherent in natural systems. To this end, fuzzy clustering methods—such as Fuzzy C-Means (FCM)—allow for partial membership assignments and are well-suited for modeling imprecise boundaries typical of geological environments [37].

1.3. Proposed hybrid DBN–FCM workflow

This study proposes a novel hybrid machine learning workflow that combines DBN and FCM for geothermal prospectivity mapping in Northeastern Nigeria. The model integrates

Landsat-derived thermal and vegetation indices with aeromagnetic data to capture both surface and subsurface geothermal signatures. The workflow involves:

1. DBN Feature Extraction: DBN is used to extract meaningful patterns and features from the input dataset, reducing dimensionality while preserving critical information.

2. FCM Clustering: The extracted features are then clustered using FCM, which accommodates uncertainty and fuzzy boundaries in the geological data.

1.4. Significance and advantages of the approach

- Robust Feature Learning: DBN's deep architecture enhances feature representation by learning high-level abstractions from noisy and complex datasets.

- Fuzzy Handling of Uncertainty: FCM's probabilistic clustering approach effectively captures the imprecise and gradational nature of geothermal prospect zones.

- Improved Predictive Accuracy: The synergy between DBN and FCM improves clustering quality and interpretability, leading to more reliable geothermal potential maps.

1.5. Location and geology of the study area

The study area is located primarily within Bauchi State, with portions extending into Plateau and Gombe States (Figure 1). It is bounded by longitudes 9° 00'E to 11° 00'E and latitudes 9 ° 30'N to 11 ° 00'N. The area spans 12 geological map sheets: Kailatu (127), Madaki (128), Ganjuwa (129), Dukku (130), Toro (148), Bauchi (149), Alkaleri (150), Ako

(151), Maijuju (169), Balewa (170), Yuli (171), and Futuk (172). Geologically, the region encompasses a transition from the Precambrian Basement Complex to Cretaceous and Tertiary sedimentary formations (Figure 2). The western part is predominantly underlain by the Precambrian Basement Complex, which includes migmatite-gneiss, granite gneiss, and biotite granite—products of the Pan-African orogeny that exhibit significant metamorphic and structural features [28, 38]. The area lies along the northeastern margin of the West African Rift System, marking a transitional zone between the Jos Plateau's crystalline basement and the sedimentary cover of the Cretaceous–Tertiary Benue Basin. The Upper Benue Trough (UBT), a Cretaceous rift system formed during the separation of Africa and South America [39], dominates the region. The regional structural grain trends NE–SW, reflecting early Cretaceous rift–rift–transform interactions that segmented the West African Craton [40, 41]. The Gongola Basin, part of the UBT, features a stratigraphic succession that reflects a transition from continental to marine and back to continental depositional environments. From oldest to youngest, the formations include the Bima, Yolde, Pindiga, Gombe, and Kerri-Kerri Formations—each with distinct lithologies and depositional settings. Beneath the sedimentary cover lies the Pan-African Basement Complex (ca. 600–500 Ma), composed of high-grade migmatite–gneiss, metasedimentary belts, and Older Granite intrusions, including equigranular biotite-hornblende granites, fine- to coarse-grained biotite granites, charnockites, quartz syenites, and subordinate gabbros [28, 42]. These granites were emplaced during the late Pan-African orogeny and display a variety of textures, from porphyritic to medium-grained hornblende-biotite granites [43]. The region is also intruded by Mesozoic "Younger Granite" ring complexes (ca. 200–120 Ma), which include granite porphyry, rhyolitic ignimbrites, and associated microgranites. These anorogenic intrusions exploited pre-existing NE–SW and NW–SE basement lineaments, forming zoned ring dykes and cone sheets [42]. Geochemically, the Younger Granites are enriched in radiogenic elements such as uranium, thorium, and potassium, yielding high heat production rates of up to $3.35 \ \mu \ Wm^{-3}$ and locally elevated basal heat flow [44]. In the adjacent Benue Trough, heat flow values range from 70 to 90 mWm^{-2}—anomalously high for a cratonic region—and are attributed, in part, to radiogenic heat production from these intrusions [45]. Table 1 shows the key lithologies in the study area and their geothermal relevance.

2. Materials and method

This study employed remote sensing, geological, and geophysical datasets to extract geothermal prospectivity parameters (GPPs). These parameters were analyzed using a Deep Belief Network (DBN) to derive latent features, which were then clustered using Fuzzy C-Means (FCM) clustering. The clustering results were used to produce a geothermal prospectivity map of the study area.
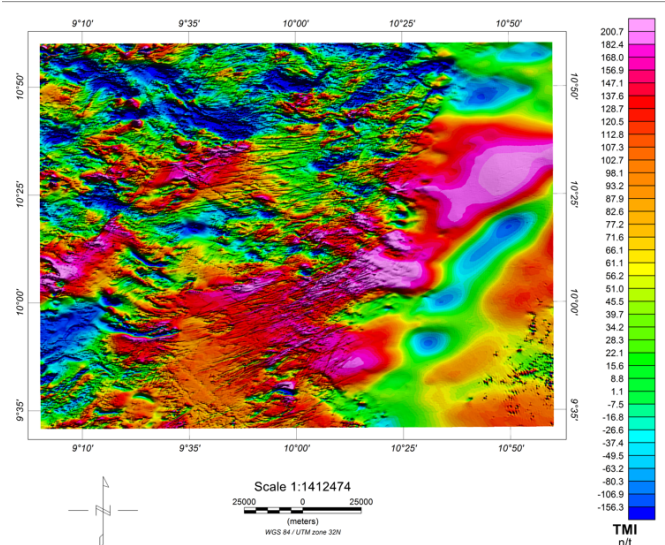

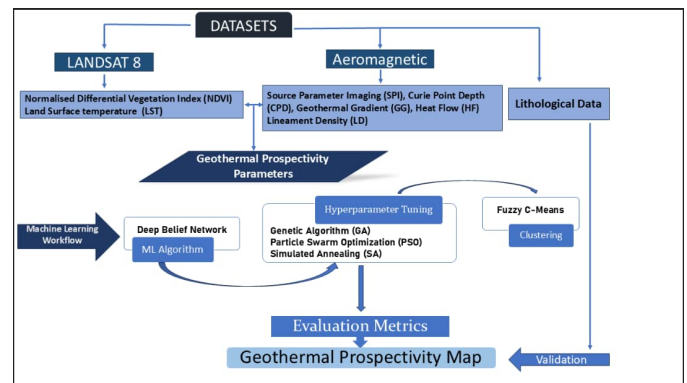Figure 3. Total Magnetic Intensity (TMI) map of the study area.

Figure 4. Workflow diagram.

2.1. Materials

The datasets utilized include Landsat 8 imagery, airborne magnetic data, and geological maps. Level 1 Landsat 8 Operational Land Imager and Thermal Infrared Sensor scenes were obtained from United State Geological Survey EarthExplorer for the path/row combinations 187/052, 187/053, 186/052, 186/053, and 188/053, acquired between February 3 and 5, 2024. The scenes were mosaicked into a single image and clipped to the study area using ArcGIS and ENVI software. Standard preprocessing steps, including radiometric and atmospheric corrections, were applied to enhance data quality. Aeromagnetic data were sourced from the Nigerian Geological Survey Agency (NGSA). The data, acquired by Fugro Airborne Surveys between 2004 and 2009, covers twelve geological map sheets: Kailatu (127), Madaki (128), Ganjuwa (129), Dukku (130), Toro (148), Bauchi (149), Alkaleri (150), Ako (151), Maijuju (169), Balewa (170), Yuli (171), and Futuk (172). The dataset had undergone preliminary corrections prior to public release [46]. Additional processing in this study included Reduction to the Equator and Regional-Residual Separation, conducted using the Oasis Montaj platform (Figure 3).

Table 1. Key lithologies in the study area and their geothermal relevance.

Lithology	Age/Origin	Key characteristics	Geothermal relevance
Rhyolite	Mesozoic Younger Granite (120–200 Ma)	Felsic, volcanic; often associated with hydrothermal systems	High heat production; common host for geothermal reservoirs
Ignimbrite	Mesozoic	Welded volcanic tuff; high silica content	High porosity and radiogenic heat generation potential
Biotite hornblende granite	Pan-African Basement (ca. 600 Ma)	Coarse-grained intrusive rock rich in radiogenic elements (U, Th, K)	Source of radiogenic heat; structurally fractured
Charnockite / granite gneiss / granulite	Precambrian	High-grade metamorphic rocks with variable mineralogy	High thermal conductivity and residual heat capacity
Syenite–quartz syenite–gabbro	Pan-African Basement	Intermediate–mafic intrusive suite	Structural permeability; moderate heat production
Migmatite / migmatite gneiss	Precambrian	Mixed metamorphic–igneous complex	Moderate heat flow; fracture networks possible
Kerri–Kerri Formation (with Wikki Warm Spring)	Tertiary sedimentary	Mostly sandstone; overlying basement heat sources	Known surface geothermal manifestation (Wikki Warm Spring)

2.2. Methods

Figure 4 below shows a brief algorithmic workflow diagram from preprocessing → DBN → FCM → validation.

2.2.1. Geothermal prospectivity parameters derivation

The GPPs used in this study were derived from airborne magnetic data and Landsat 8 bands 4, 5, and thermal bands. These parameters include the Normalized Difference Vegetation Index (NDVI), land surface temperature (LST), source parameter imaging (SPI), CPD, geothermal gradient (GG), and HF. These GPPs have been extensively used in geothermal resource exploration by various authors [26, 27, 47].

The extracted parameters from Landsat imagery reveal surface manifestations of geothermal resources. The NDVI was computed using atmospherically corrected bands 4 and 5. The NDVI was calculated using the following Eq. (1):

$$NDVI = \frac{Band5 - Band4}{Band5 + Band4}. \tag{1}$$

The LST was extracted using thermal bands 10 and 11. The temperature was retrieved in ENVI software using the Emissivity Reference Channel method. This method assumes that emissivity remains constant across all pixels within a single thermal infrared band [48]. Using this constant emissivity, a temperature image is generated using the Planck function [49]. The Planck function used is represented in Eq. (2):

$$T_R = \frac{C_2}{\lambda_R \ln\left(\frac{\epsilon_R C_1}{L_R \lambda_R^5 \pi} + 1\right)}, \tag{2}$$

where T_R is the land surface temperature (K) retrieved from the reference channel, λ_R is the Wavelength of the reference channel (μm), ϵ_R is the emissivity of the reference channel, L_R is the radiance measured in the reference channel (W/m^2/sr/μm), and C_1, C_2 are the Planck constants.

The SPI technique interprets the total magnetic intensity (TMI) by calculating its second-order derivatives to form an analytical signal. From this, a local wave number k is obtained, which is independent of the source's susceptibility contrast, dip, and regional geomagnetic parameters [50]. The depth z to the top of a magnetic source is then estimated by Eqs. (3) and (4):

$$z = \frac{1}{k}, \tag{3}$$

$$\kappa = \frac{1}{A^2}\left[\frac{\partial^2 T}{\partial x \partial z}\frac{\partial T}{\partial x} + \frac{\partial^2 T}{\partial y \partial z}\frac{\partial T}{\partial y} - \left(\frac{\partial^2 T}{\partial x^2} + \frac{\partial^2 T}{\partial y^2}\right)\frac{\partial T}{\partial z}\right], \tag{4}$$

$$A^2 = \left(\frac{\partial T}{\partial x}\right)^2 + \left(\frac{\partial T}{\partial y}\right)^2 + \left(\frac{\partial T}{\partial z}\right)^2 ,$$

where T is the total magnetic intensity, $\partial T/\partial x$, $\partial T/\partial y$, and $\partial T/\partial z$ are the three orthogonal derivatives, and A is the analytical signal [51].

Similarly, the Total Magnetic Intensity (TMI) was used as the basis for the extraction of structural lineaments. The residual-corrected grid was enhanced through derivative filtering using the Geosoft Oasis Montaj MAGMAP tool. A total horizontal derivative accentuates magnetic gradients in all directions, sharpening the edges of faults and fractures by highlighting abrupt changes in magnetization. The enhanced derivative grids were then exported to a GIS environment for lineament delineation, where linear features were manually digitized by tracing continuous high-gradient trends guided by tonal and textural variations. To quantify spatial distribution and connectivity, the resulting lineaments were analyzed using ArcGIS's Kernel Density tool, producing density maps that highlight corridors of structural permeability—key controls on geothermal fluid flow.

The spectral analysis method was employed for estimating depths, including CPD, GG, HF. To achieve this, the residual grid was subjected to an overlapping block window approach, dividing the area into thirty-five (35) equal square blocks. The radial power spectrum algorithm was applied to calculate the spectral data of each block. CPD refers to the depth at which a ferromagnetic material loses its magnetism, and the temperature at this depth is called the Curie Temperature or Curie Point (T_c). A graph of the logarithm of power was plotted against frequency (radians per km) to estimate the CPD (Z_b) of the magnetic source. The depth to the top of the magnetic source, Z_t, is derived from the slope of the low-frequency segment of the logarithmic power spectrum, while the centroid depth, Z_0, is calculated by normalizing the spectral amplitude by the absolute wavenumber (k) and fitting a straight line to the segment corresponding to the lowest wavenumbers. The depth to the top of the magnetic source (Z_t) and centroid depth (Z_0) were estimated using Eqs. (5) and (6), respectively.

$$\ln |P|k||^{1/2} = \ln B - |k|Z_t , \tag{5}$$

$$\ln\left(\frac{[P|k|]^{1/2}}{|k|}\right) = \ln D - |k|Z_o , \tag{6}$$

$$Z_b = 2Z_o - Z_t, \tag{7}$$

where B is a constant, Z_t is the depth to the top of the magnetic source, and $\left[\ln |P_k|^{1/2}\right]$ is the radially averaged power spectrum, D is a constant. Subsequently, the CPD, Z_b, is determined using Eq. (7) after [52].

The geothermal gradient (GG), dT/dZ, quantifies the increase in temperature with depth beneath the Earth's surface, reflecting the conductive heat flow from the planet's interior toward its exterior. Above the Curie temperature, both induced and remanent magnetizations are lost in ferromagnetic materials. However, beyond approximately 580 °C, many crustal minerals begin to deform ductility. Consequently, the Curie
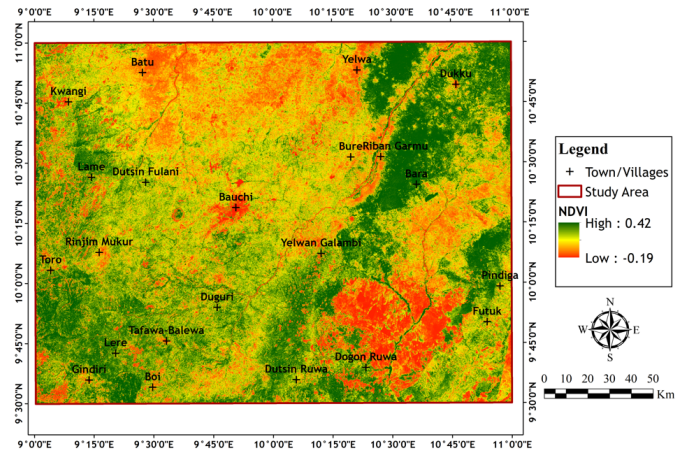

Figure 5. Normalized differential vegetation index (NDVI) map of the study area..

temperature is typically assumed to be 580°C. Together with the CPD measurement, this value is used to estimate the GG using Eq. (8) [53].

$$\frac{dT}{dZ} = \frac{580°C}{Z_b}. \tag{8}$$

The heat flow (HF), q, values are calculated by multiplying the geothermal gradient by the thermal conductivity of rocks, as shown in Eq. (9).

$$q = k\frac{dT}{dZ}, \tag{9}$$

Where q is the heat flow and k is the coefficient of thermal conductivity. Thermal conductivity (k) typically varies with local lithology. An average value of 2.5 $Wm^{-1}°C^{-1}$ was used, as the study area is dominated by igneous rocks [21].

2.2.2. Mathematical and conceptual framework of the machine learning algorithms used

The core of the methodology is a Deep Belief Network (DBN), which learns hierarchical feature representations through stacked Restricted Boltzmann Machines (RBMs). Each RBM is an undirected probabilistic model consisting of visible units v and hidden units h, and is trained using contrastive divergence to approximate the data distribution [35]. RBM is defined by an energy function, as shown in Eq. (10) [54]

$$E(v,h) = -\sum_i \sum_j v_i w_{ij} h_j - \sum_i a_i v_i - \sum_j b_j h_j. \tag{10}$$

Layers are added greedily: after one RBM converges, its hidden activations become the visible data for the next RBM, enabling deep architectures to overcome vanishing gradients. During pretraining, an L_2 weight-decay regularization term $\lambda\|W\|^2$ is applied to each RBM's weight matrix to prevent overfitting and promote smoother feature extraction [55]. The final hidden-layer activations constitute the latent features that are fed into the clustering stage. Hyperparameter tuning of the RBM layers (e.g., number of components, learning rates) is achieved using metaheuristic optimization algorithms:

- Genetic Algorithm (GA): Inspired by natural evolution, GA maintains a population of candidate hyperparameter "chromosomes," applying selection, crossover, and mutation operators to evolve toward higher fitness—defined here as improved clustering quality—over successive generations [56].

- Particle swarm optimization (PSO): This method models a swarm of particles navigating the hyperparameter space. Each particle updates its velocity and position by balancing personal experience and social learning to converge on optimal solutions [57].

- Invasive weed optimization: Mimicking the colonization behaviour of weeds, this algorithm allows individuals to produce seeds in proportion to their fitness. Seeds are dispersed spatially, with variance reducing over time, and population control is applied to retain only the fittest individuals—allowing robust exploration of complex, nonlinear search spaces [58, 59].

Clustering is then performed using the Fuzzy C-Means (FCM) algorithm, which partitions the latent features into ccc clusters by minimizing the objective function defined in Eq. (11) [60].

$$ J = \sum_{i=1}^{n} \sum_{j=1}^{c} u_{ij}^{m} \left\| x_i - c_j \right\|^2 , \qquad (11) $$

where $u_{ij} \in [0, 1]$ is the membership degree of point x_i in cluster j, c_j is the j-th cluster center, and $m > 1$ is the fuzzifier controlling cluster softness. Memberships and cluster centers c_j are updated iteratively via Eqs. (12) and (13) until convergence, allowing points to belong partially to multiple clusters and thus modeling uncertainty in the feature space.

$$ u_{ij} = \left[\sum_{k=1}^{c} \left(\frac{\| x_i - c_j \|}{\| x_i - c_k \|} \right)^{\frac{2}{m-1}} \right]^{-1} , \qquad (12) $$

$$ c_j = \frac{\sum_{i=1}^{n} u_{ij}^{m} x_i}{\sum_{i=1}^{n} u_{ij}^{m}} . \qquad (13) $$

This ensures that points closer to a cluster center have higher membership values in that cluster. The objective function weights each data point by its fuzzy membership degree. Convergence is typically achieved when changes in membership values fall below a predefined threshold or after reaching a maximum number of iterations. The choice of the fuzzifier m (commonly m=2) balances cluster overlap and crispness: lower values of mmm yield sharper, more distinct clusters, while higher values allow for greater ambiguity in membership [61]. FCM's soft assignment strategy is particularly valuable in geospatial applications such as geothermal prospectivity mapping, where boundaries between geological facies are inherently uncertain [62].

2.2.3. Implementation of the machine learning algorithm

Prior to model training, a 1 km × 1 km fishnet grid was generated over the study area, and its centroids were used to extract all geothermal prospectivity parameters from the raster layers using the "Extract Multi Values to Points" tool in ArcGIS. The resulting multivariate point feature class, containing values for all predictors, was then exported as a CSV file. This CSV dataset served as the input for machine learning implementation in Jupyter Lab. A Deep Belief Network (DBN) was constructed to learn robust latent feature representations from the normalized input data. Preprocessing involved MinMax normalization [63], scaling all features to the [0, 1] range to ensure equal weighting. The DBN architecture consisted of stacked Bernoulli Restricted Boltzmann Machines (RBMs), where each layer was regularized using L2 (weight decay) to prevent overfitting and enhance generalization [35]. During pretraining, data were passed through the RBMs layer-by-layer, with each layer transforming the input into increasingly abstract latent representations. To evaluate how well the DBN captured the underlying structure of the data, a backward pass was performed: latent features were reconstructed using transposed weight matrices and a sigmoid activation function. The quality of the reconstruction was assessed using Mean Squared Error (MSE) and Kullback–Leibler (KL) divergence, which quantify the reconstruction error and the divergence between original and reconstructed probability distributions, respectively. Hyperparameter tuning of the DBN (e.g., number of neurons, learning rates) was performed using metaheuristic optimization techniques, including placeholder implementations of Genetic Algorithms (GA), Particle Swarm Optimization (PSO), and Simulated Annealing (SA). These methods searched for parameter configurations that minimized reconstruction error and improved clustering performance. The final latent representations were clustered using Fuzzy C-Means (FCM), which provided both hard cluster assignments (via maximum membership) and a Fuzzy Partition Coefficient (FPC) to measure the degree of cluster separation. Standard clustering metrics—including Silhouette Score, Davies–Bouldin Index, Partition Coefficients (Fuzzy and Modified), and the Xie–Beni Index—were computed to evaluate clustering performance. To determine the optimal number of clusters, a grid search was conducted over cluster counts ranging from 3 to 10. For each configuration, validity indices such as the Silhouette Index, Partition Coefficient (PC), and Classification Entropy (CE) were used to assess clustering quality. The optimal cluster count was selected based on the best trade-off between compactness and separation. Combined, the reconstruction metrics (MSE and KL divergence) and clustering validity indices offer a comprehensive evaluation of DBN's feature learning capabilities and the quality of the resulting cluster structures. This pipeline provides a robust framework for unsupervised feature learning, hyperparameter optimization, and cluster validation in geothermal prospectivity analysis.

2.2.4. Validation

To validate the machine learning–based geothermal prospectivity map, lithological units within the study area were cross-analyzed with the final cluster-based geothermal potential classes. Lithological data were compiled from existing geological maps and literature, and subsequently grouped according to

Table 2. Evaluation metrics for different cluster counts.

Clusters	Silhouette score	Partition coefficient	Classification entropy
3	0.5793	0.9134	0.1493
4	0.5458	0.8963	0.1805
5	0.5483	0.8936	0.1858
6	0.5443	0.8926	0.1893
7	0.5268	0.8837	0.2045
8	0.5266	0.8837	0.2054
9	0.5165	0.8777	0.2155
10	0.5202	0.8787	0.2142

their geological ages, ranging from the Quaternary to the Precambrian. The percentage distribution of each lithological unit across the geothermal prospectivity classes was computed using spatial overlay analysis within a GIS environment. This involved intersecting the classified prospectivity map with the lithological layer and calculating the proportion of each lithology falling within each prospectivity class. To statistically assess the relationship between lithology and geothermal potential, a Chi-square test of independence was performed. This test evaluated whether the observed distribution of lithological units across the geothermal prospectivity clusters significantly deviated from a random distribution.

3. Results and discussion

3.1. Geothermal prospectivity parameters results

3.1.1. Normalized difference vegetation index (NDVI)

The normalized difference vegetation index (NDVI) quantifies vegetation 'greenness' and health, with values typically ranging from –1 (indicating no vegetation) to +1 (indicating dense vegetation). In geothermal exploration, low NDVI anomalies often coincide with subsurface thermal activity, such as elevated soil temperatures that can stress vegetation, leading to detectable NDVI depressions [64, 65]. Figure 5 presents the NDVI map of the study area, with values ranging from –0.19 to 0.42. The central and southeastern zones—near Bauchi, Rinjim Mukur, and Dogon Ruwa—show NDVI values below 0, indicating sparse or stressed vegetation, which may be associated with underlying geothermal conduits. In contrast, the northwestern and eastern margins exhibit NDVI values greater than 0.3, reflecting healthy, undisturbed vegetation cover. Such NDVI anomalies have been successfully correlated with heat discharge estimations in several case studies [66, 67].

3.1.2. Land surface temperature

Figure 6 shows the LST distribution across the study area, with values ranging from 16.34 °C to 64.63 °C. Elevated LSTs (>32.63 °C) are concentrated in the central and southeastern sectors—particularly around Bauchi, Rinjim Mukur, and Dogon Ruwa—which may indicate geothermal heat loss from underlying subsurface reservoirs. In contrast, the northwestern and western margins exhibit lower temperatures (< 27.70 °C), likely due to dense vegetation cover that insulates the surface.
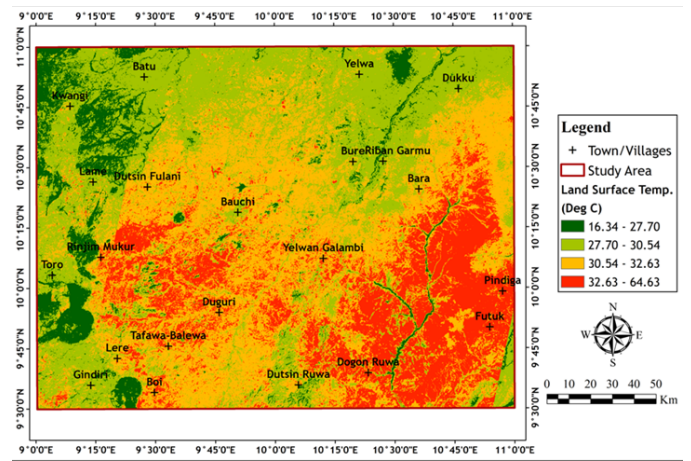

Figure 6. LST map of the study area.

These high-temperature anomalies often coincide with structural conduits that channel geothermal fluids. However, as noted by Sayao [68], LST readings can also be influenced by urban surfaces, bare soils, or moisture deficits. Therefore, it is essential to corroborate LST anomalies with additional indicators before making inferences about geothermal potential.

3.1.3. Source parameter imaging

The SPI map of the study area reveals depth values ranging from 24 m (shallow) to 6125 m (deep), as shown in Figure 7. Most of the region exhibits shallow SPI values (<718m), indicating proximity to near-surface geological features. Notably, deeper SPI values (> 1579m) are concentrated in the eastern part of the study area, around towns such as Bara, Dogon Ruwa, Dukku, and Pindiga. These deeper SPI values, typically within the sedimentary domain, suggest a thick sedimentary cover separating the surface from the magnetic basement—ranging from several hundred meters to a few kilometers. This thickness acts as a thermal blanket, reducing conductive heat flux to the surface and suppressing geothermal gradients, thereby masking potential deep heat sources [69]. Additionally, such deep sources often occur beneath broad, low-slope sedimentary depocenters, where limited fluid circulation and low reservoir permeability reduce their viability for shallow geothermal exploitation [70]. In contrast, SPI depths of less than ~718 m in the basement complex domain typically indicate shallow magnetic sources—such as fractured granites or volcanic intrusions—located just beneath the weathered zone [69]. These shallow sources are frequently associated with high heat-producing granitic bodies characterized by elevated radiogenic heat generation and high thermal conductivity.

3.1.4. Lineament density

The lineament density in the study area ranges from 0 to 0.1 km/km^2 (Figure 8). The central, western, and northern parts of the study area, around Batu, Kwangi, Dutsin Fulani, Bauchi, Yelwan Galambi, and Bure Ribban Garmu, exhibit dense fracture networks, indicating structurally complex zones with potentially elevated permeability. In contrast, the southern and

Table 3. Comparative evaluation metrics for FCM and DBN-based clustering workflows.

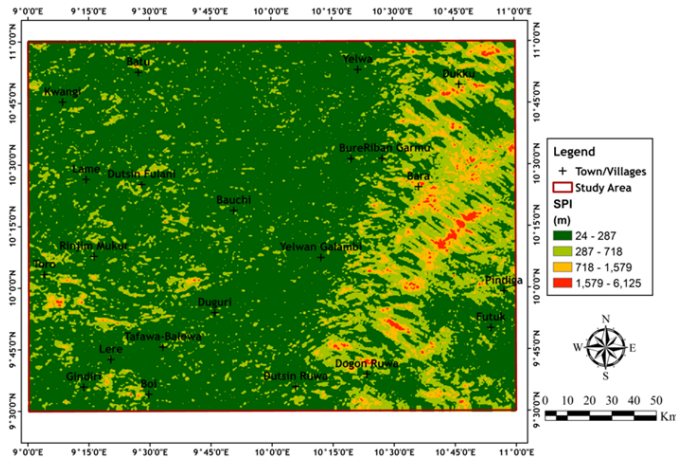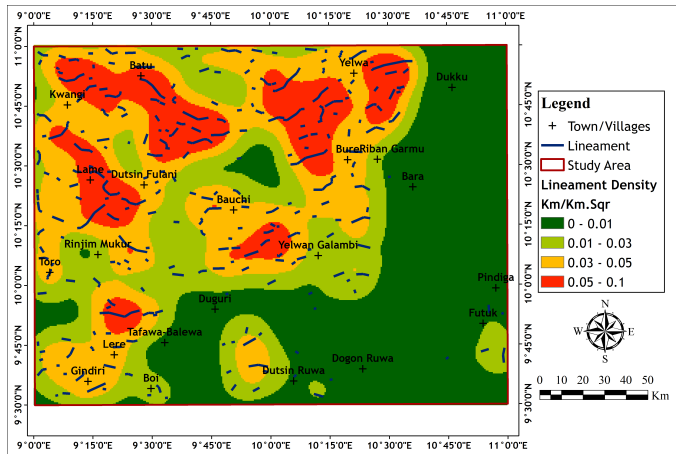| Metrics	FCM on Raw Data	DBN Baseline + FCM	DBN GA + FCM	DBN PSO + FCM	DBN SA + FCM
Silhouette score	0.3379	0.5793	0.5806	0.5801	0.5810
Davies–Bouldin index	1.0663	0.5111	0.5095	0.5099	0.5095
FPC	0.8029	0.9134	0.9140	0.9135	0.9146
MPC	0.7044	0.8702	0.8710	0.8703	0.8719
Xie–Beni index	0.2960	0.0913	0.0908	0.0910	0.0903

Figure 7. SPI map of the study area.

Figure 8. Lineament density map of the study area.

eastern margins show sparse lineaments, suggesting fewer fluid pathways. High lineament density zones have been shown to correlate with enhanced permeability and fluid pathways in geothermal fields. Studies by Saepuloh [71], Tende [72], and Rafiq [73] demonstrated a strong positive association between high lineament density and known geothermal occurrences, emphasizing its value in geothermal resource assessment.

3.1.5. Curie point depth

The CPD indicates the depth at which rocks lose magnetization (580 °C). In our study (Figure 9), CPD values range from 8.22 km (shallow) to 27.8 km (deep), revealing pronounced lat-

eral thermal contrasts. Shallow CPD zones (8.22–12.75 km) cluster around Batu, Yelwa, Lere, and Tafawa Balewa, suggesting anomalously high geothermal potential [21, 45]. Conversely, deeper CPD values (> 20 km) prevail near Pindiga, Futuk, and Dukku.

3.1.6. Geothermal gradient

The geothermal gradient quantifies the temperature increase per kilometer of depth and governs reservoir productivity. As shown in Figure 10, gradients range from 20.85 °C/km (low) to 70 °C/km (high). Steep gradients (>55.61 °C/km) are observed along the northern belt (Batu, Yelwa) and the southwestern flank (Tafawa Balewa, Gindiri, Lere, Boi), marking zones of rapid temperature rise conducive to geothermal resource accumulation [21, 47]. In contrast, gentler gradients (<33.25 °C/km) in the southeast (Futuk, Pindiga, Dogon Ruwa, Duguri), east (Bara), and west (Toro, Dutsin Fulani) suggest limited viability.

3.1.7. Heat flow HF

Heat flow measures the conductive flux of thermal energy from the crust into the overlying layers [21]. As shown in Figure 11, moderate (111–133 mW/m^2) to high (>133 mW/m^2) heat-flow values dominate the northern, central, and southwestern sectors of the study area, with isolated peaks in the north and southwest. Such elevated heat-flow regions have been identified as prime geothermal targets [21, 45]. Radiogenic heat production—resulting from the decay of uranium, thorium, and potassium in basement granites—can generate sustained thermal anomalies in the upper crust [44]. Additionally, shallow magmatic intrusions facilitated by tectonic structures may locally enhance heat flow through advective transfer [26]. Together, these processes explain the spatial distribution of heat-flow highs and underscore their significance for geothermal exploration.

3.2. Machine learning results

3.2.1. Cluster number selection

Selecting an appropriate number of clusters is critical to balancing the capture of meaningful geothermal prospectivity patterns against the risk of overfitting noise. We evaluated clustering solutions ranging from three to ten clusters using three internal validity metrics—Silhouette Score, Partition Coefficient (PC), and Classification Entropy (CE)—for the Fuzzy C-Means (FCM) clustering applied to DBN-extracted features. The results are summarized in Table 2. As shown in Table 2, the
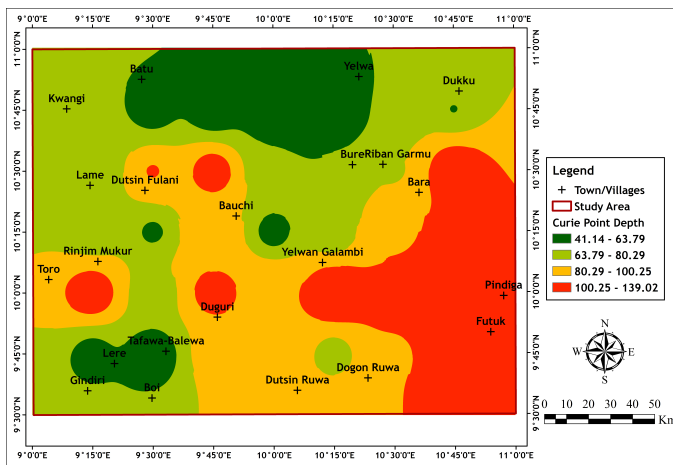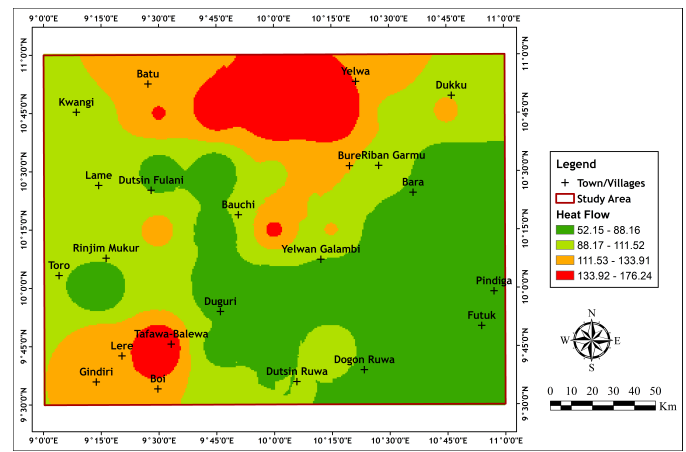
Figure 9. Curie dept point map of the study area.

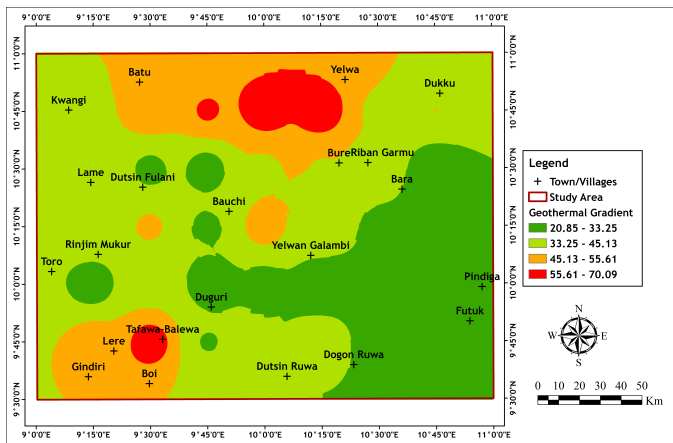

Figure 11. HF map of the study area.

Figure 10. GG map of the study area.

cal inputs, (2) a Deep Belief Network (DBN) baseline followed by FCM, and DBN variants optimized using (3) Genetic Algorithm (GA), (4) Particle Swarm Optimization (PSO), and (5) Simulated Annealing (SA) (Table 3). Each workflow was assessed using five internal validity metrics: Silhouette Score, Davies–Bouldin Index, Fuzzy Partition Coefficient (FPC), Modified Partition Coefficient (MPC), and Xie–Beni Index.

When applied to the raw feature space (e.g., NDVI, lineament density, LST), FCM produced suboptimal results: the Silhouette Score was low (0.3379), indicating that many data points lie close to or between clusters, and the Davies–Bouldin Index was high (1.0663), reflecting considerable overlap and dispersion among groups. The FPC (0.8029) and MPC (0.7044) indicated moderate crispness, suggesting significant ambiguity in membership assignments. Additionally, the relatively large Xie–Beni Index (0.2960) confirmed high intra-cluster scatter relative to inter-cluster separation. These findings are consistent with previous observations that FCM struggles to delineate well-separated clusters when applied directly to raw geospatial features [78]. In contrast, applying FCM to latent features extracted via a DBN significantly enhanced clustering performance. The Silhouette Score increased by over 70% to 0.5793 (a >70% increase), and the Davies–Bouldin Index was nearly halved to 0.5111, indicating more compact and well-separated clusters. Membership crispness also improved markedly (FPC = 0.9134, MPC = 0.8702), and the Xie–Beni Index dropped to 0.0913, reflecting substantially reduced fuzzy compactness. Similar performance boosts have been documented in image-based clustering studies where deep feature embeddings greatly improve cluster definition prior to fuzzy partitioning [79].

Further refinements were achieved by optimizing DBN hyperparameters via metaheuristic algorithms. All three optimizers—GA, PSO, and SA—delivered incremental yet consistent gains over the untuned DBN baseline. Silhouette Scores slightly improved to around 0.5805, with SA achieving the highest score (0.5810). The Davies–Bouldin Index marginally decreased to 0.5095, while FPC (0.9146) and MPC (0.8719) sharpened cluster boundaries. The Xie–Beni Index also im-

3-cluster configuration achieves the highest Silhouette Score (0.5793), reflecting a superior balance between intra-cluster cohesion and inter-cluster separation [74]. It also yields the highest PC value (0.9134), indicating crisp and well-defined fuzzy groupings [75, 76], and the lowest CE (0.1493), suggesting minimal cluster overlap [75, 77].

By contrast, increasing k beyond three steadily degrades all three metrics: Silhouette Scores fall below 0.55, PC drops below 0.90, and CE rises above 0.18, indicating declining cluster quality and increasing ambiguity. The superior metric values at k=3 imply that the latent feature space naturally partitions into three distinct geothermal prospectivity classes—low, moderate, and high. Higher-order segmentation (e.g., five or more clusters) introduces fragmentation without meaningful differentiation, while fewer clusters (e.g., k=2) risk oversimplification. Therefore, the 3-cluster solution optimally balances interpretability and analytical rigor for delineating geothermal target zones in the study area.

3.2.2. Machine learning algorithms evaluation metrics results

In this study, we evaluated five clustering workflows: (1) Fuzzy C-Means (FCM) applied directly to raw geophysi-

Table 4. Geothermal prospectivity parameters statistics by cluster and ranking.

Cluster No.	NDVI	LST (°C)	SPI (m)	LD (km/km^2)	CPD (km)	GG (°C/km)	HF (mW/m^2)	Prospectivity Rank
0	0.1461	30.59	258	0.0268	16.05	39.58	98.95	2
1	0.1393	32.45	363	0.00595	20.82	29.59	73.99	1
2	0.1399	29.47	190	0.0533	12.65	49.85	124.64	3

Table 5. Percentage distribution of geothermal prospectivity across lithological units.

Lithology	Low (%)	Moderate (%)	High (%)
Alluvium	86.91	4.85	8.24
Kerrikerri Formation	61.16	28.66	10.18
Gombe Formation	48.93	32.38	18.69
Pindiga Formation	100	0.00	0.00
Yola Formation	100	0.00	0.00
Bima Formation	100	0.00	0.00
Quartz porphyry	0.00	72.78	27.22
Granite and granite porphyry	0.00	100.	0.00
Ignimbrite	0.00	46.24	53.76
Rhyollite	0.00	18.92	81.08
Biotite hornblende–Granite Syenite, Quartz	3.50	96.50	0.00
Syenite and Gabbro Fine-grained	0.00	45.25	54.75
Biotite granite Coarse porphyritic	0.46	53.92	45.62
Biotite granite	14.93	27.35	57.71
Charnokitic Rocks	1.01	44.68	54.30
Muscovite Quartz Schist	100.	0.00	0.00
Granite gneiss	7.32	47.69	44.99
Granulite and Gneiss	0.00	24.28	75.72
Biotite Granite	3.60	45.70	50.70
Migmatite Gneiss	17.24	55.71	27.05
Migmatite	25.04	64.37	10.59

proved slightly, reaching its lowest at 0.0903 with SA. While these gains were smaller than those introduced by DBN itself, they demonstrate the value of fine-tuning. Among the methods, SA yielded the most geologically coherent and statistically robust clusters. Overall, the tighter, well-separated, and less ambiguous clusters generated by the optimized DBN models offer greater reliability for delineating zones of geothermal prospectivity.

3.2.3. Cluster feature statistics, ranking and interpretation

After finalizing the three-cluster solution, we computed the mean values of each geothermal prospectivity parameter within each cluster (Table 4) and visualized the clusters in 3D space using Principal Component Analysis (Figure 12). Clusters were then ranked from 1 to 3 (1 = lowest, 2 = moderate, 3 = highest) based on the mean value of the first latent feature (PC1) in each FCM partition. This ranking provides a consistent, data-driven ordering of clusters along the primary latent dimension extracted by the DBN. Cluster 2, ranked highest (Rank 3), ex-

hibits the shallowest CPD with a mean of only 12.65 km, indicating higher subsurface temperatures and an elevated heat flow regime [21]. It also records the highest geothermal gradient (49.86 °C/km) and surface heat flow (124.65 mW/m^2), both well above typical continental averages, reflecting an excellent deep thermal resource [44]. The lowest mean SPI depth (190 m) suggests minimal deep-seated magnetic contrasts, while the highest lineament density (0.053 km/km^2) points to a well-developed fracture network conducive to fluid flow and heat extraction. Interestingly, despite these favorable subsurface conditions, this cluster has the lowest mean LST (29.47 °C) and a relatively low NDVI (0.140). This counterintuitive combination may result from persistent soil moisture or seasonal vegetation cover that suppresses daytime surface warming, even in regions of high geothermal potential. These characteristics make Cluster 2 the most promising target for conventional geothermal exploitation. Cluster 0, ranked moderate (Rank 2), shows an intermediate CPD (16.06 km), a geothermal gradient of 39.58 °C/km, and heat flow of 98.96 mW/m^2. Its SPI depth (258.4 m) indicates moderately shallow magnetic sources, and its lineament density (0.0268 km/km^2) suggests a somewhat developed fracture network. It also has the highest mean NDVI (0.146) and a mid-range LST (30.60 °C), reflecting healthier vegetation and moderate surface heating—consistent with a transitional zone between high-potential basement rocks and deeper sedimentary cover. Cluster 1, ranked lowest (Rank 1), is characterized by the deepest CPD (20.82 km), the gentlest geothermal gradient (29.60 °C/km), and the lowest heat flow (73.99 mW/m^2). Its high SPI depth (363 m) points to deep-seated magnetic sources, while the minimal lineament density (0.00595 km/km^2) indicates poor structural permeability. The highest mean LST (32.46 °C) and moderate NDVI (0.139) likely reflect arid, sparsely vegetated surfaces rather than elevated geothermal activity. Cluster 2's combination of shallow CPD, steep geothermal gradient, elevated heat flow, and dense structural permeability makes it the most prospective geothermal target zone. Cluster 0 represents a moderate potential zone, while Cluster 1—with its deep CPD and low heat flow—is the least favorable. This ranking aligns with established geothermal exploration criteria [21, 26, 45, 47]. Figure 12 presents a three-dimensional projection of the DBN-derived latent features onto the first three principal components (PC1, PC2, and PC3), with each point colored by its assigned cluster and annotated by prospectivity rank (Cluster 1/Rank 1 = blue, Cluster 0/Rank 2 = red, Cluster 2/Rank 3 = green). Along PC1, which captures the greatest variance and is driven primarily by geothermal gradient and heat flow, a clear left-to-right ordering of clusters emerges—progressing from low (blue), through
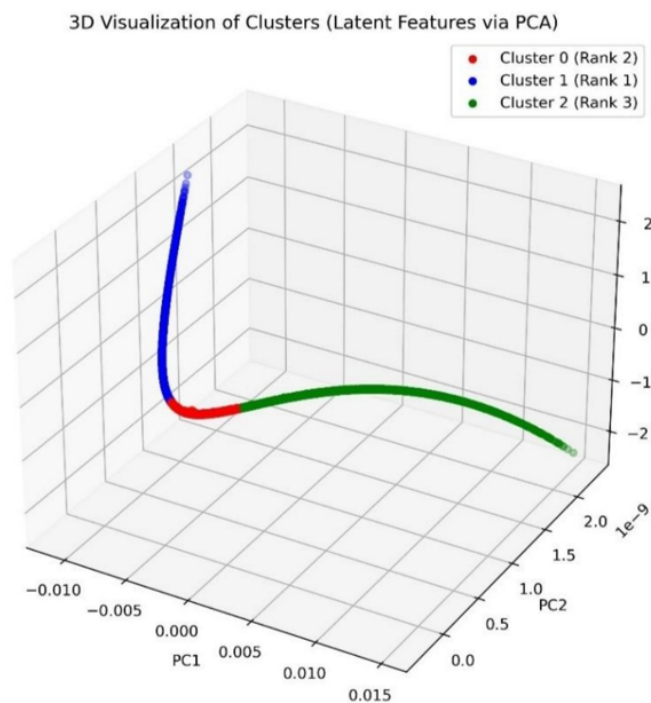
Figure 12. 3D visualization of cluster latent features via principal component analysis.

moderate (red), to high prospectivity (green). This strong separation along PC1 validates the ranking scheme and reflects the optimal Silhouette Score achieved with k = 3. Meanwhile, PC2 (vertical axis) and PC3 (depth axis) introduce subtler, orthogonal distinctions likely governed by secondary variables such as NDVI or lineament density, without compromising the thermal-based cluster separation along PC1. The tight, non-overlapping "streams" of each color confirm the compactness and cohesion of each cluster, supporting the robustness of the three-cluster solution. These patterns demonstrate that the principal latent features extracted by the DBN effectively differentiate geothermal prospectivity zones. The ranking from blue (low) through red (moderate) to green (high) aligns well with the unsupervised PCA structure, reinforcing confidence in both the clustering methodology and its geoscientific interpretation.

3.3. Geothermal prospectivity map

The final geothermal prospectivity map (Figure 13), generated using the best-performing DBN model optimized via Simulated Annealing (SA), delineates the study area into three classes: low (red), moderate (yellow), and high (green) potential. Spatially, low-potential zones cover 32.3% ($\approx$ 11,779 km^2), moderate zones cover 35.0% ($\approx$12,764 km^2), and high-potential zones comprise 32.7% ($\approx$ 11,926 km^2). The high-potential areas are concentrated primarily in the northwestern, southwestern, and scattered central parts of the study area. These coincide with exposures of crystalline basement rocks and known structural lineaments (e.g., around Batu, Gindiri, and Lere). These regions exhibit shallow Curie Point

Depths, steep geothermal gradients, and elevated heat-flow values, validating their classification as high-prospectivity targets. Moderate-potential zones form a continuous central band linking Bauchi, Dutsin Fulani, and Rinjim Mukur, as well as transitional belts in the eastern sector near Dukku and Bara. These areas are characterized by intermediate thermal signatures and mixed lithological covers. The presence of the Wikki Warm Spring, located in a moderate-potential enclave within the Kerri-Kerri Formation, further supports the model's capacity to detect local geothermal anomalies beneath sedimentary layers. The Wikki Warm Spring, with a temperature of 32°C [47], represents a low-temperature geothermal resource, and its placement in the moderate-prospectivity zone is geologically justified. Low-potential areas dominate the eastern margins (around Pindiga and Futuk) and appear as isolated patches near Rinjim Mukur and Duguri. These regions are characterized by thick sedimentary cover and deep Curie depths, which collectively suppress conductive heat flow. The nearly equal areal distribution of low and high prospectivity zones—alongside a slightly larger moderate band—reflects a balanced spatial pattern of favorable and unfavorable thermal regimes across the study area. The DBN–SA optimized clustering has thus produced a robust, spatially coherent geothermal prospectivity framework that aligns well with known geothermal manifestations.

3.4. Validation of geothermal prospectivity using lithological distribution

Validation of the geothermal prospectivity map was carried out by analyzing lithological associations with the resulting clusters. Table 5 summarizes the distribution of geothermal potential classes (low, moderate, and high) across various lithologies, as derived from the machine learning clustering process. A horizontal stacked bar chart (Figure 14) visually represents this distribution, highlighting key patterns. From Table 5, it is evident that certain lithologies exhibit a strong affinity for high prospectivity. For instance, Rhyolite shows the highest concentration in the high-potential zone (81.08%), followed by Granulite and Gneiss (75.72%), and Ignimbrite (53.76%). These findings align well with geological expectations, as rhyolites and ignimbrites are typically associated with volcanic and subvolcanic systems that serve as effective heat sources [80, 81]. Likewise, the high heat retention and radiogenic potential of granulite-grade metamorphic rocks are particularly significant in regions with suspected or confirmed geothermal activity [82]. Notably, some Pan-African basement rocks such as Charnockitic rocks, fine-grained biotite granite, and syenite–quartz syenite–gabbro also exhibit substantial representation in the high prospectivity class (exceeding 45%). This reinforces their known radiogenic heat generation potential and structural favorability for geothermal systems. Abul Khair [83] emphasized that deeply fractured granites—and by extension, gneisses—can serve as viable Enhanced Geothermal System (EGS) candidates due to their inherent heat-producing and transmissive properties. Interestingly, certain younger sedimentary formations, particularly the Gombe and Kerri-Kerri Formations, also show notable proportions in the moderate to
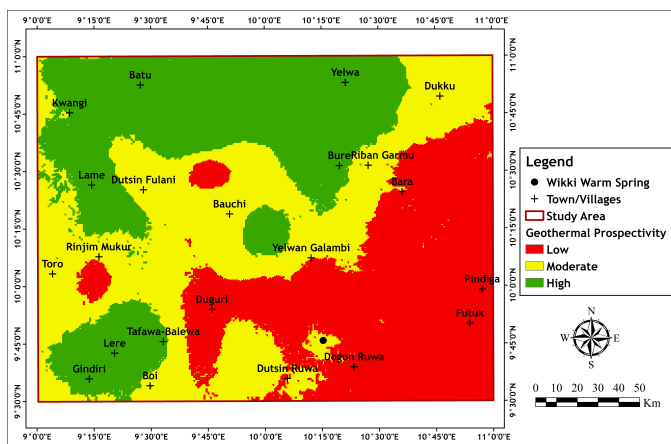
Figure 13. Geothermal prospectivity map of the study area.

Figure 14. Stacked bar chart of geothermal prospectivity distribution across lithological units (by percentage).

high prospectivity classes (32.38% and 10.18%, respectively). This supports earlier findings that geothermal anomalies can occur within sedimentary basins, where deep meteoric water circulation or underlying intrusive bodies contribute to localized thermal anomalies. The presence of the Wikki Warm Spring, geologically located within the Kerri-Kerri Formation, further corroborates the moderate thermal signature recorded in this unit. This observation strengthens the argument that while geothermal activity in sedimentary environments is atypical, it can still be significant where favorable heat sources and permeability structures (e.g., faults) are present [84].

Conversely, lithologies such as Alluvium, Pindiga, Yola, and Bima Formations overwhelmingly fall into the low prospectivity class (over 86–100%). This is consistent with expectations, as these units primarily consist of unconsolidated or low-thermal-conductivity sediments, which are poor conductors of heat and generally thermally inert. To statistically validate the relationship between lithology and geothermal prospectivity classes, a Chi-square test was conducted, yielding a result of $\chi^2 = 16261.28$, with a p-value < 0.0001. This highly significant outcome confirms that the spatial distribution of geothermal potential is not random with respect to lithology, but rather statistically dependent, further validating the clustering outcomes of the machine learning model. In summary, lithological distribution lends strong support to the credibility of the machine-learned geothermal prospectivity classes. Both known heat-generating lithologies (e.g., rhyolite, ignimbrite) and field evidence (e.g., Wikki Warm Spring in the Kerri-Kerri Formation) correspond well with the high and moderate prospectivity zones. Therefore, the integrated approach combining Deep Belief Networks (DBN), Fuzzy C-Means (FCM), and geophysical inputs proves effective in delineating geologically meaningful geothermal targets.

4. Conclusion

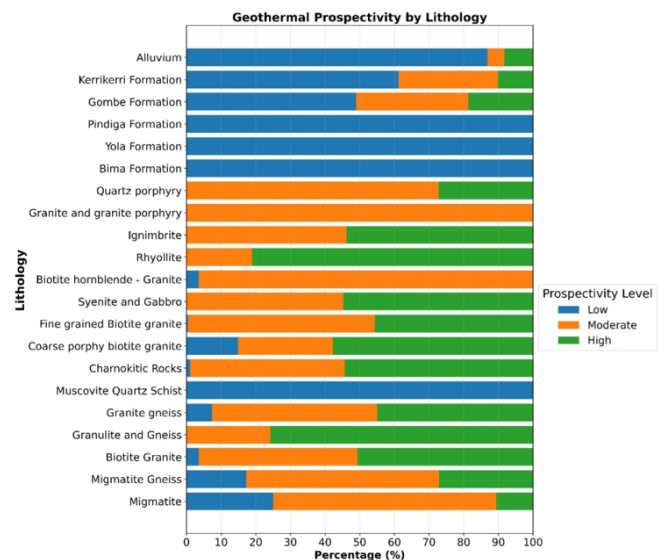To advance exploratory geothermal prospectivity mapping, we evaluated five clustering workflows: raw-input Fuzzy C-Means (FCM), DBN-derived FCM (DBN-FCM), and Deep Belief Network variants optimized via Genetic Algorithm (DBN-GA), Particle Swarm Optimization (DBN-PSO), and Simulated Annealing (DBN-SA). These models were applied to key geothermal prospectivity parameters extracted via GIS from remotely sensed and geophysical datasets. Among them, the DBN-SA workflow achieved the best internal validity, effectively partitioning the study area into low, moderate, and high prospectivity zones. Clustering on latent features enhanced Silhouette Scores by over 70% and halved the Davies–Bouldin Index compared to the raw-input FCM approach. The high-prospectivity cluster, covering 32.7% of the area, is characterized by the shallowest Curie Point Depth, steepest geothermal gradient, shallow magnetic source depth, highest heat flow, and greatest lineament density. Our DBN-SA model delineates coherent thermal corridors that align with the Wikki Warm Spring and are enriched in hot lithologies (rhyolite, ignimbrite, granulite), as confirmed by a significant Chi-square association. This reproducible workflow offers a robust foundation to guide field surveys and prioritize drilling in both basement-controlled terrains and sedimentary basins.

Future work should incorporate additional constraints such as structural controls and geochemical anomalies to refine target delineation and test the DBN-SA schema across varied tectonic settings. Scaling this multi-parameter, deep-feature learning strategy across underexplored regions will help validate its global applicability and accelerate sustainable geothermal development, particularly in areas where surface manifestations are scarce.

Data availability

The data used for this paper will be made available upon request.

Acknowledgment

References

[1] S. O. Oyedepo, "Energy and sustainable development in Nigeria: the way forward", Energy, Sustainability and Society **2** (2012) 15. https://doi.org/10.1186/2192-0567-2-15.

[2] E. M. Abraham & E. E. Nkitnam, "Review of geothermal energy research in Nigeria: the geoscience front", International Journal of Earth Sciences and Geophysics **3** (2017) 15. https://vibgyorpublishers.org/content/ijesg/fulltext.php?aid=ijesg-3-015.

[3] S. Lo Russo, G. Taddia & V. Verda, "Development of the thermally affected zone (TAZ) around a groundwater heat pump (GWHP) system: a sensitivity analysis", Geothermics **43** (2012) 66. https://doi.org/10.1016/j.geothermics.2012.02.001.

[4] A. I. Osman, L. Chen, M. Yang, G. Msigwa, M. Farghali, S. Fawzy, D. W. Rooney & P. S. Yap, "Cost, environmental impact, and resilience of renewable energy under a changing climate: a review", Environmental Chemistry Letters **21** (2023) 741. https://doi.org/10.1007/s10311-022-01532-8.

[5] K. A. Mogaji, O. T. Adeniyi & A. A. Komolafe, "Geothermal energy potentiality modeling using GIS-based machine learning algorithm concept in southwestern Nigeria: insights from geophysical and remote sensing data sets", Research Square (2023). https://doi.org/10.21203/rs.3.rs-3089187/v1.

[6] J. A. Mono, T. Ndougsa Mbarga, Y. Tarek, J. D. Ngoh & I. O. Amougou, "Estimation of Curie-point depths, geothermal gradients and near-surface heat flow from spectral analysis of aeromagnetic data in the Loum–Minta area (centre-east Cameroon)", Egyptian Journal of Petroleum **27** (2018) 1291. https://doi.org/10.1016/j.ejpe.2018.07.002.

[7] S. T. A. Okolie, O. Ozuor, O. Fakehinde, S. O. Ongbali, O. S. I. Fayomi & F. A. Agu, "Study of Nigeria geothermal energy resources viability, brief production techniques and transportation", Energy Procedia **157** (2019) 1475. https://doi.org/10.1016/j.egypro.2018.11.312.

[8] M. F. Coolbaugh, C. Kratt, A. Fallacaro, W. M. Calvin & J. V. Taranik, "Detection of geothermal anomalies using advanced spaceborne thermal emission and reflection radiometer (ASTER) thermal infrared images at Bradys Hot Springs, Nevada, USA", Remote Sensing of Environment **106** (2007) 350. https://doi.org/10.1016/j.rse.2006.09.001.

[9] E. M. Abraham, K. M. Lawal, A. C. Ekwe, O. Alile, K. A. Murana & A. A. Lawal, "Reply to discussion on spectral analysis of aeromagnetic data for geothermal energy investigation of Ikogosi Warm Spring, Ekiti State, southwestern Nigeria", Geothermal Energy **2** (2014) 18. https://doi.org/10.1186/s40517-014-0018-9.

[10] Q. Lv, Y. Dou, X. Niu, J. Xu & B. Li, *Classification of land cover based on deep belief networks using polarimetric RADARSAT-2 data*, Proceedings of the IEEE Geoscience and Remote Sensing Symposium (IGARSS) Quebec City, QC, Canada, 2014, pp. 4679–4682. https://doi.org/10.1109/IGARSS.2014.6947537.

[11] S. Li, B. Jiang, S. Liang, J. Peng, H. Liang, J. Han & K. Jia, "Evaluation of nine machine learning methods for estimating daily land surface radiation budget from MODIS satellite data", International Journal of Digital Earth **15** (2022) 1784. https://doi.org/10.1080/17538947.2022.2130460.

[12] Y. Wei, H. Zhang, J. Dai, R. Zhu, L. Qiu, Y. Dong & S. Fang, "Deep belief network with swarm spider optimization method for renewable energy power forecasting", Processes **11** (2023) 1001. https://doi.org/10.3390/pr11041001.

[13] K.-T. T. Bui, D. T. Bui, J. Zou, C. Van Doan & I. Revhaug, "A novel hybrid artificial intelligent approach based on neural fuzzy inference model and particle swarm optimization for horizontal displacement modeling of hydropower dam", Neural Computing and Applications **29** (2018) 1495. https://doi.org/10.1007/s00521-016-2666-0.

[14] K. Sörensen & F. W. Glover, "Metaheuristics", in Encyclopedia of operations research and management science, S. I. Gass & M. C. Fu (Eds.), Springer, Boston, MA, (2013) 960. https://doi.org/10.1007/978-1-4419-1153-7_1167.

[15] S. Shamshirband, M. Hadipoor, A. Baghban, A. Mosavi, J. Bukor & A. R. Várkonyi-Kóczy, "Developing an ANFIS–PSO model to predict mercury emissions in combustion flue gases", Mathematics **7** (2019) 965. https://doi.org/10.3390/math7100965.

[16] L. I. Nwankwo, "Estimation of depths to the bottom of magnetic sources and ensuing geothermal parameters from aeromagnetic data of Upper Sokoto Basin, Nigeria", Geothermics **54** (2015) 76. https://doi.org/10.1016/j.geothermics.2014.12.001.

[17] L. I. Nwankwo & A. T. Shehu, "Evaluation of Curie point depths, geothermal gradients and near surface heat flow from high-resolution aeromagnetic (HRAM) data of the entire Sokoto Basin, Nigeria", Journal of Volcanology and Geothermal Research **305** (2015) 45. https://doi.org/10.1016/j.jvolgeores.2015.09.017.

[18] T. O. Lawal & L. I. Nwankwo, "Evaluation of the depth to the bottom of magnetic sources and heat flow from high-resolution aeromagnetic (HRAM) data of part of Nigeria sector of Chad Basin", Arabian Journal of Geosciences **10** (2017) 378. https://doi.org/10.1007/s12517-017-3154-2.

[19] J. O. Adedapo, E. Kurowska, K. Schoeneich & A. E. Ikpokonte, "Geothermal gradient of the Niger Delta from recent studies", International Journal of Scientific and Engineering Research **4** (2013) 39. https://docslib.org/doc/2212118/geothermal-gradient-of-niger-delta-from-recent-studies.

[20] G. O. Emujakporue & A. S. Ekine, "Determination of geothermal gradient in the Eastern Niger Delta sedimentary basin from bottom hole temperatures", Journal of Earth Sciences and Geotechnical Engineering **4** (2014) 109. https://www.researchgate.net/publication/315678417.

[21] G. E. Obande, K. M. Lawal & L. A. Ahmed, "Spectral analysis of aeromagnetic data for geothermal investigation of Wikki Warm Spring, north-east Nigeria", Geothermics **50** (2014) 85. https://doi.org/10.1016/j.geothermics.2013.08.002.

[22] S. Kasidi & A. Nur, "Estimation of Curie point depth, heat flow and geothermal gradient inferred from aeromagnetic data over Jalingo and environs, north-eastern Nigeria", International Journal of Scientific Engineering and Technology **6** (2013) 294. https://www.researchgate.net/publication/288016929.

[23] M. Y. Kwaya, E. Kurowska & A. S. Arabi, "Geothermal gradient and heat flow in the Nigeria sector of the Chad Basin, Nigeria", Computer Water, Energy and Environmental Engineering **5** (2016) 70. https://doi.org/10.4236/cweee.2016.52007.

[24] C. G. Chukwu, E. E. Udensi, E. M. Abraham, A. C. Ekwe & A. O. Selemo, "Geothermal energy potential from analysis of aeromagnetic data of part of the Niger-Delta Basin, southern Nigeria", Energy **143** (2018) 846. https://doi.org/10.1016/j.energy.2017.11.040.

[25] O. Sunday, A. A. Elijah, B. O. Samuel & C. O. Daramola, "Investigation of geothermal potential of the Dahomey basin, Nigeria, through analysis of geomagnetic and geo-resistivity dataset", NRIAG Journal of Astronomy and Geophysics **11** (2022) 373. https://doi.org/10.1080/20909977.2022.2141022.

[26] A. K. Usman, J. Osumeje, Y. A. Bello, Y. A. Hassan & E. Onuh, "Evaluation of geothermal energy resource potential in northeastern Nigeria using spectral analysis of aeromagnetic data", Scientific World Journal **20** (2025) 122. https://doi.org/10.4314/swj.v20i1.16.

[27] A. K. Usman, J. Osumeje, K. Lawal, Y. A. Hassan & M. Umar, "A preliminary assessment of north-eastern Nigeria's geothermal potential zones using land surface temperature", Scientific World Journal **20** (2025) 445. https://doi.org/10.4314/swj.v20i1.60.

[28] N. G. Obaje, *Geology and mineral resources of Nigeria*, Springer, 2009. https://doi.org/10.1007/978-3-540-92685-6.

[29] M. H. Dickson & M. Fanelli, *Geothermal energy: utilization and technology*, Routledge, 2003. https://doi.org/10.4324/9781315065786.

[30] E. R. Okoroafor, C. M. Smith, K. I. Ochie, C. J. Nwosu, H. Gudmundsdottir & M. Aljubran, "Machine learning in subsurface geothermal energy: two decades in review", Geothermics **102** (2022) 102401. https://doi.org/10.1016/j.geothermics.2022.102401.

[31] M. Boumehdi, Y. Hahou, K. Amrouch, N. E. Berkat, J. Carneiro, A. Correia & O. Sadki, "New assessment of geothermal resources in Morocco: evaluation of the Curie point depth method using magnetic data for geothermal gradient and heat flow estimation", Scientific African **28** (2025) e02726. https://doi.org/10.1016/j.sciaf.2025.e02726.

[32] Z. Naseer, M. Ehsan, M. Ali, M. R. Amjad, M. A. U. Latif & K. Abdelrahman, "Lithofacies and sandstone reservoir characterization for geother-

mal assessment through artificial intelligence", Results in Engineering **26** (2025) 105173. https://doi.org/10.1016/j.rineng.2025.105173.

[33] H. Guo, C. Li, B. Peng, X. Shan, J. Xu, Z. Zhang & J. Chang, "Geothermal regime and its implication on hydrocarbon accumulation in the northern Junggar Basin", Geological Journal (2025). https://doi.org/10.1002/gj.5194.

[34] F. Khan, M. Mahmoud, A. Raza, M. Murtaza, B. N. Tackie-Otoo, S. Patil, T. Al Shafloot & M. S. Kamal, "Laboratory demonstration of geothermal rock cooling to reduce breakdown pressure in hydraulic fracturing", presented at GOTECH Conference, Dubai, UAE, 2025. https://doi.org/10.2118/224657-MS.

[35] G. E. Hinton, S. Osindero & Y. W. Teh, "A fast-learning algorithm for deep belief nets", Neural Computation **18** (2006) 1527. https://doi.org/10.1162/neco.2006.18.7.1527.

[36] Y. Bengio, "Learning deep architectures for AI", Foundations and Trends in Machine Learning **2** (2009) 1. https://doi.org/10.1561/2200000006.

[37] J. C. Bezdek, R. Ehrlich & W. Full, "FCM: The fuzzy c-means clustering algorithm", Computers & Geosciences **10** (1984) 191. https://doi.org/10.1016/0098-3004(84)90020-7.

[38] M. N. Tijani, "Geology of Nigeria", in *Landscapes and landforms of Nigeria*, A. Faniran, L. K. Jeje, O. A. Fashae & A. O. Olusola (Eds.) Springer, Cham, 2023. https://doi.org/10.1007/978-3-031-17972-3_1.

[39] J. B. Wright, "The Benue Trough and coastal basins", in *Geology and mineral resources of West Africa*, J. B. Wright (Ed.) Springer, Dordrecht, 1985. https://doi.org/10.1007/978-94-015-3932-6_11.

[40] A. Mamudua, E. S. Akanbia & S. C. Odewumi, "Hydrothermal alteration and mineral potential zones of Bauchi area northeastern Nigeria using interpretation of aeroradiometric data", Journal of the Nigerian Society of Physical Sciences **7** (2025) 2193. https://doi.org/10.46481/jnsps.2025.2193.

[41] J. G. Fitton, "The Cameroon Line, West Africa: A comparison between oceanic and continental alkaline volcanism", in Alkaline igneous rocks, J. G. Fitton & B. G. J. Upton (eds.), Geological Society, London, Special Publications **30** (1987) 273. https://doi.org/1144/GSL.SP.1987.030.01.13.

[42] T. Schlüter, "Review of countries and territories", in *Geological atlas of Africa*, Springer, Berlin and Heidelberg, 2008, p. 31. https://doi.org/10.1007/978-3-540-76373-4_4.

[43] A. Oyebamiji, O. Akinola, O. Olaolorun, Y. Abdu-Raheem, A. Adeoye & M. Oguntuase, "Geochemistry, petrogenesis and geological implication of granitic rocks in Igarra area, southwestern Nigeria", Applied earth science **133** (2024) 174. https://doi.org/10.1177/25726838241273519.

[44] A. B. Yusuf, H. S. Lim & I. Ahmad Abir, "Radiogenic heat production estimation towards sustainable energy drive in northeastern Nigeria", Heliyon **9** (2023) e16310. https://doi.org/10.1016/j.heliyon.2023.e16310.

[45] K. Salako, A. Abbass, A. Rafiu, U. Alhassan, A. Aliyu & A. Taiwo, "Assessment of geothermal potential of parts of Middle Benue Trough, north-east Nigeria", Journal of environmental soil physics **45** (2020) 27. https://doi.org/10.22059/jesphys.2019.260257.1007017.

[46] O. M. Adedokun, O. P. Oladejo, K. N. Alao, E. O. Adeniyi, H. Otobrise, K. O. Suleman, T. A. Adagunodo, O. Adedokun & L. A. Sunmonu, "Delineation of structural lineaments of Shaki West southwestern Nigeria using high resolution aeromagnetic data", Journal of the Nigerian Society of Physical Sciences **7** (2025) 2493. https://doi.org/10.46481/jnsps.2025.2493.

[47] A. Yusuf, L. H. San & I. A. Abir, "A preliminary geothermal prospectivity mapping based on integrated GIS, remote-sensing, and geophysical techniques around northeastern Nigeria", Sustainability **13** (2021) 8525. https://doi.org/10.3390/su13158525.

[48] V. Caselles, E. Valor, C. Coll & E. Rubio, "Thermal band selection for the PRISM instrument: Analysis of emissivity–temperature separation algorithms", Journal of Geophysical Research: Atmospheres **102** (1997) 11145. https://doi.org/10.1029/97JD00344.

[49] P. S. Kealy & S. J. Hook, "Separating temperature and emissivity in thermal infrared multispectral scanner data: implications for recovering land surface temperatures", IEEE Transactions on Geoscience and Remote Sensing **31** (1993) 1155. https://doi.org/10.1109/36.317447.

[50] S. J. Alhadithi & A. S. Al-Banna, "Using source parameter imaging technique to the aeromagnetic data to estimate the basement depth of Tharthar Lake and surrounding area in Central Iraq", Iraqi Geological Journal **55** (2022) 151. https://doi.org/10.46717/igj.55.1F.12Ms-2022-06-27.

[51] J. B. Thurston & R. S. Smith, "Automatic conversion of magnetic data to depth, dip, and susceptibility contrast using the SPI method", Geophysics **62** (1997) 807. https://doi.org/10.1190/1.1444190.

[52] Y. Okubo, R. J. Graf, R. O. Hansen, K. Ogawa & H. Tsu, "Curie point depths of the Island of Kyushu and surrounding areas, Japan", Geophysics **50** (1985) 481. https://doi.org/10.1190/1.1441926.

[53] A. Tanaka, Y. Okubo & O. Matsubayashi, "Curie point depth based on spectrum analysis of the magnetic anomaly data in East and Southeast Asia", Tectonophysics **306** (1999) 461. https://doi.org/10.1016/S0040-1951(99)00072-4.

[54] G. E. Hinton, "A practical guide to training restricted Boltzmann machines", in Neural Networks: Tricks of the Trade, Lecture Notes in Computer Science **7700**, Springer, Berlin and Heidelberg, 2012, p. 599. https://doi.org/10.1007/978-3-642-35289-8_32.

[55] A. Fischer & C. Igel, "An introduction to restricted Boltzmann machines", in *Progress in Pattern Recognition, Image Analysis, Computer Vision, and Applications*, L. Alvarez, M. Mejail, L. Gomez & J. Jacobo (Eds.) Lecture Notes in Computer Science **7441**, Springer, Berlin and Heidelberg, 2012, p. 14. https://doi.org/10.1007/978-3-642-33275-3_2.

[56] J. H. Holland, "Genetic algorithms and adaptation", in *Adaptive Control of Ill-Defined Systems*, O. G. Selfridge, E. L. Rissland & M. A. Arbib (Eds.) NATO Conference Series **16**, Springer, Boston, MA, 1984, p. 317. https://doi.org/10.1007/978-1-4684-8941-5_21.

[57] J. Kennedy, "Particle swarm optimization", in *Encyclopedia of Machine Learning*, C. Sammut & G. I. Webb (Eds.) Springer, Boston, MA, 2011, p. 760. https://doi.org/10.1007/978-0-387-30164-8_630.

[58] A. Mehrabian & C. Lucas, "A novel numerical optimization algorithm inspired from weed colonization", Ecological Informatics **1** (2006) 355. https://doi.org/10.1016/j.ecoinf.2006.07.003.

[59] K. Su, L. Ma, X. Guo & Y. Sun, "An efficient discrete invasive weed optimization algorithm for web services selection", Journal of Software **9** (2014) 709. https://doi.org/10.4304/jsw.9.3.709-715.

[60] J. C. Dunn, "A fuzzy relative of the ISODATA process and its use in detecting compact well-separated clusters", Journal of Cybernetics **3** (1973) 32. https://doi.org/10.1080/01969727308546046.

[61] J. C. Bezdek, *Pattern recognition with fuzzy objective function algorithms*, Springer, Boston, MA, 1981. https://doi.org/10.1007/978-1-4757-0450-1.

[62] V. Schwämmle & O. N. Jensen, "A simple and fast method to determine the parameters for fuzzy c–means cluster analysis", Bioinformatics **26** (2010) 2841. https://doi.org/10.1093/bioinformatics/btq534.

[63] F. Pedregosa, G. Varoquaux, A. Gramfort, V. Michel, B. Thirion, O. Grisel, M. Blondel, A. Müller, J. Nothman, G. Louppe, P. Prettenhofer, R. Weiss, V. Dubourg, J. Vanderplas, A. Passos, D. Cournapeau, M. Brucher, M. Perrot & É. Duchesnay, "Scikit-learn: machine learning in Python", Journal of Machine Learning Research **12** (2011) 2825. https://jmlr.csail.mit.edu/papers/v12/pedregosa11a.html.

[64] N. Zaini, M. Yanis, F. Abdullah, F. van der Meer & M. Aufaristama, "Exploring the geothermal potential of Peut Sagoe volcano using Landsat 8 OLI/TIRS images", Geothermics **105** (2022) 102499. https://doi.org/10.1016/j.geothermics.2022.102499.

[65] E. Rahimi, P. Dong & C. Jung, "Global NDVI–LST correlation: temporal and spatial patterns from 2000 to 2024", Environments **12** (2025) 67. https://doi.org/10.3390/environments12020067.

[66] S. Guha & H. Govil, "Land surface temperature and normalized difference vegetation index relationship: a seasonal study on a tropical city", SN Applied Sciences **2** (2020) 1661. https://doi.org/10.1007/s42452-020-03458-8.

[67] N. Kikon, D. Kumar & S. A. Ahmed, "Quantitative assessment of land surface temperature and vegetation indices on a kilometer grid scale", Environmental Science and Pollution Research **30** (2023) 107236. https://doi.org/10.1007/s11356-023-27418-y.

[68] V. M. Sayão, N. V. dos Santos & W. de Sousa Mendes, "Land use/land cover changes and bare soil surface temperature monitoring in southeast Brazil", Geoderma Regional **22** (2020) e00313. https://doi.org/10.1016/j.geodrs.2020.e00313.

[69] S. E. Ekwok, O.-I. M. Achadu, A. E. Akpan, A. M. Eldosouky, C. H. Ufuafuonye, K. Abdelrahman & D. Gómez-Ortiz, "Depth estimation of sedimentary sections and basement rocks in the Bornu Basin, northeast Nigeria using high-resolution airborne magnetic data", Minerals **12** (2022) 285. https://doi.org/10.3390/min12030285.

[70] K. N. Alao, O. P. Oladejo, K. O. Suleman, O. Mary, E. O. Adeniyi, H.

Otobrise & L. A. Sunmonu, "Determination of depth to magnetic sources using source parameter imaging of high-resolution aeromagnetic data of Esie, north central Nigeria", International Journal of Advanced Multidisciplinary Research and Studies **4** (2024) 1091. https://doi.org/10.62225/2583049X.2024.4.6.3559.

[71] E. Júlíusson & G. Axelsson, "Stock models for geothermal resources", Geothermics **72** (2018) 249. https://doi.org/10.1016/j.geothermics.2017.11.006.

[72] A. W. Tende, M. D. Aminu & J. N. Gajere, "A spatial analysis for geothermal energy exploration using bivariate predictive modelling", Scientific Reports **11** (2021) 19755. https://doi.org/10.1038/s41598-021-99244-6.

[73] J. Rafiq, I. S. Abu-Mahfouz, K. Chavanidis, D. Arrofi & P. Soupios, "Spatial distribution of structural lineaments in the Al-Lith geothermal field, western Saudi Arabia: remote sensing and aeromagnetic data analysis", Journal of Asian Earth Sciences: X **13** (2025) 100191. https://doi.org/10.1016/j.jaesx.2025.100191.

[74] P. J. Rousseeuw, "Silhouettes: a graphical aid to the interpretation and validation of cluster analysis", Journal of Computational and Applied Mathematics **20** (1987) 53. https://doi.org/10.1016/0377-0427(87)90125-7.

[75] J. C. Bezdek, R. Ehrlich & W. Full, "FCM: the fuzzy c-means clustering algorithm", Computers & Geosciences **10** (1983) 191. https://doi.org/10.1016/0098-3004(84)90020-7.

[76] A. Starczewski, "A new validity index for crisp clusters", Pattern Analysis and Applications **20** (2017) 687. https://doi.org/10.1007/s10044-015-0525-8.

[77] H. Wang, J. Wang & G. Wang, "A survey of fuzzy clustering validity evaluation methods", Information Sciences **618** (2022) 270. https://doi.org/10.1016/j.ins.2022.11.010.

[78] K. Wu & J. Liu, "Learning large-scale fuzzy cognitive maps under limited resources", Engineering Applications of Artificial Intelligence **116** (2022) 105376. https://doi.org/10.1016/j.engappai.2022.105376.

[79] X. Wu, Y. Yu, L. Chen, W. Ding & Y. Wang, "Robust deep fuzzy K-means clustering for image data", Pattern Recognition **153** (2024) 110504. https://doi.org/10.1016/j.patcog.2024.110504.

[80] M. Halder, D. Paul & S. Sensarma, "Rhyolites in continental mafic large igneous provinces: petrology, geochemistry and petrogenesis", Geoscience Frontiers **12** (2021) 53. https://doi.org/10.1016/j.gsf.2020.06.011.

[81] S. Burchardt, M. Bazargan, E. Bessi Gestsson, C. Hieronymus, E. Ronchin, H. Tuffen, M. J. Heap, J. Davidson, B. Kennedy, A. Hobé & E. Saubin, "Geothermal potential of small sub-volcanic intrusions in a typical Icelandic caldera setting", Volcanica **5** (2022) 477. https://doi.org/10.30909/vol.05.02.477507.

[82] I. M. Artemieva, H. Thybo, K. Jakobsen, N. K. Sørensen & L. S. Nielsen, "Heat production in granitic rocks: global analysis based on a new data compilation GRANITE2017", Earth-Science Reviews **172** (2017) 1. https://doi.org/10.1016/j.earscirev.2017.07.003.

[83] H. Abul Khair, D. Cooke & M. Hand, "Seismic mapping and geomechanical analyses of faults within deep hot granites, a workflow for enhanced geothermal system projects", Geothermics **53** (2015) 46. https://doi.org/10.1016/j.geothermics.2014.04.007.

[84] A. Comerford, A. Fraser-Harris, G. Johnson & C. McDermott, "Controls on geothermal heat recovery from a hot sedimentary aquifer in Guardbridge, Scotland: field measurements, modelling and long term sustainability", Geothermics **76** (2018) 125. https://doi.org/10.1016/j.geothermics.2018.07.004.